LA-UR-19-21430 (Accepted Manuscript)

The impact of chemical order on defect transport in mixed pyrochlores

Uberuaga, Blas P.
Perriot, Romain Thibault
Pilania, Ghanshyam

To be published in: Physical Chemistry Chemical Physics

DOI to publisher's version: 10.1039/C8CP07597B

Permalink to record: http://permalink.lanl.gov/object/view?what=info:lanl-repo/lareport/LA-UR-19-21430

Cite this: DOI: 10.1039/xxxxxxxxxx

The impact of chemical order on defect transport in mixed pyrochlores†

Blas P. Uberuaga [a], Romain Perriot [a,b], and Ghanshyam Pilania [a]

Received Date
Accepted Date

DOI: 10.1039/xxxxxxxxxx

www.rsc.org/journalname

Using temperature accelerated dynamics, an accelerated molecular dynamics method, we examine the relationship between composition and cation ordering and defect transport in the mixed pyrochlore $Gd_2(Ti_{1-x}Zr_x)_2O_7$, using the oxygen vacancy as a representative defect structure. We find that the nature of transport is very sensitive to the cation structure, transitioning, as a function of composition, from three-dimensional migration to two-dimensional to pseudo-one-dimensional to becoming essentially immobile before reverting back to three-dimensional as the Zr content is increased. The rates of migration are also affected by the cation structure in the various compositions. This behavior is driven by the connectivity of Ti polyhedra in the material, with more extensive networks of Ti ions leading to a greater ability of the vacancy to traverse the material. Our results indicate that the nature of transport is dictated by the cation structure of the material and that, conversely, the cation structure could be used to control transport and potentially other functionalities in mixed pyrochlores.

1 Introduction

Atomic transport is a key functionality in a wide variety of applications. From ionic conductors to materials destined for irradiation environments, high diffusion rates is one criterion that makes a material attractive. Thus, there is an ongoing effort to find materials that exhibit ever greater rates of mass transport. In the context of complex oxides, defined here as oxides with more than one cation sublattice, researchers have examined a wide variety of materials including (but certainly not limited to) perovskites[1–3] and pyrochlores[4,5]. While there are suggestions that current materials may be at or near the limit of transport rates[6], there is still a vast chemical space that has not been explored where surprises could reside. In particular, as the chemical richness of these materials is increased, new behavior can emerge that, while not necessarily leading to faster transport, can provide avenues for tailoring and controlling transport mechanisms to a greater degree.

For example, double perovskites ($AA'BB'O_6$), perovskite (ABO_3) compounds that contain more than one A or B cation, are known to order[7,8]. Depending on the chemistry, they can order in a variety of ways, with different potential orderings on the A and B sublattice. Further, this ordering is known to impact the functionality of the compound. In particular, the transport kinetics of oxygen vacancies depends on this ordering, with some orderings exhibiting higher oxygen vacancy mobilities than either end member[9]. While the impact of ordering on functionality has been extensively studied in perovskites, less effort has been devoted to other complex oxides, particularly those with even more complex structures than perovskites.

Pyrochlores ($A_2B_2O_7$) are another class of complex oxides that have received significant attention for a multitude of reasons, particularly for their potential fast ionic conductivity. High conductivity in pyrochlores arises from the effective substoichiometry of the anion sublattice. Compared to the parent fluorite (B_4O_8) structure, pyrochlores are missing oxygen ions and thus the oxygen sublattice contains structural vacancies. In pyrochlores that exhibit high degrees of cation order, such as those in which B=Ti, these structural vacancies are also strongly ordered and such compounds do not exhibit high conductivities. However, in other pyrochlores (B=Zr for example), the oxygen structural vacancies

[a] Materials Science and Technology Division, Los Alamos National Laboratory, Los Alamos, NM, USA. E-mail: blas@lanl.gov; [b] current affiliation: Theoretical Division, Los Alamos National Laboratory, Los Alamos, NM, USA.

have greater mobility and can migrate relatively quickly. This high mobility is typically connected to disorder, or mixing, on the cation sublattice. In most experimental studies, disorder is induced through chemistry. That is, disorder in a B=Ti pyrochlore is induced by adding Zr.

Recently, we found that some of these mixed pyrochlore chemistries can exhibit ordering[10]. That is, a pyrochlore such as $Gd_2(Ti_{1-x}Zr_x)_2O_7$ (GTZO) can display ordering of the Ti and Zr on the B sublattice. Interestingly, this ordering can be stabilized by a shift in oxygen atoms that create a 7-fold environment for Zr while maintaining a 6-fold environment for Ti. More importantly, however, these results suggest that mixing pyrochlore chemistries can lead to complex and non-intuitive consequences. In some cases, the mixed pyrochlores form solid solutions[11–13]. However, in others, mixing two pyrochlore chemistries leads to phase separation and a two-phase composite structure[14,15]. The samples in many experiments in which two pyrochlores are mixed to vary the level of disorder are often interpreted as random solid solutions—that there is a continuous change in behavior from one end-member chemistry to the other. That some of these compositions may exhibit strong ordering suggests that experimental interpretations may not always be so straight forward. Indeed, some experiments have seen non-monotonic changes in conductivity with changes in chemistry[16].

Thus, there is still much that is not understood regarding the interplay between local chemistry and mass transport. Even in a so-called single pyrochlore (with only one A and one B cation), the distribution of those cations can have a complex impact on defect migration[17,18]. In this work, we examine the consequences of cation ordering in mixed pyrochlores on defect transport. For simplicity, and because of the relevance to ionic conductors, we focus on the behavior of oxygen vacancies. Using accelerated molecular dynamics (AMD) simulations with classical Buckingham potentials, we find that, as the chemistry of $Gd_2(Ti_{1-x}Zr_x)_2O_7$ shifts from Ti ($x = 0$) to Zr ($x = 1$) rich compositions, different ordered structures are favored and both the rate as well as the nature of oxygen vacancy migration changes. In particular, as x is varied, oxygen vacancy migration goes from a three-dimensional diffuser, to 2D, to 1D, and back to 3D. This complex dependence on composition is attributed to the specific arrangement of Ti and Zr in the lattice.

2 Methodology

2.1 Generation of Structures

We generated ordered structures for various compositions of GTZO in two ways. First, we used canonical Monte Carlo, based on an empirical potential of the Buckingham form, to determine low energy orderings of $Gd_2(Ti_{1-x}Zr_x)_2O_7$ for $x = 0.25$, $x = 0.50$, and $x = 0.75$. The composition was held constant while the positions of Ti and Zr atoms were allowed to swap with the standard Metropolis acceptance criterion. Initially, the cations were placed at random and the Monte Carlo was performed at a temperature of 100 K for 10^5 steps. After each attempted swap of cations, the energy of the system was minimized and the Monte Carlo acceptance probability based on this energy. The total number of swaps accepted were 88, 116, and 97 in the $x = 0.25$, $x = 0.5$, and $x = 0.75$ compositions, respectively. The lattice constants of these cells were relaxed for the initial cation distribution, but then kept constant for the remainder of the simulation.

Second, for the $x = 0.75$ composition, we started with the structure we found recently using density functional theory (DFT)[10]. This structure, the most stable structure for mixed Ti/Zr Gd-based pyrochlores, is stabilized in part by the formation of 7-fold Zr-center polyhedra, in contrast to the normal 6-fold coordination of cations on the B site in pyrochlore. This occurs for very specific Zr/Ti orderings because an oxygen atom can displace, forming these 7-fold coordination polyhedra around Zr while still maintaining the 6-fold coordination of the Ti cations. Starting with this structure, we first orthogonalized it[19] (the structure found via DFT was not fully orthorhombic) and then minimized it with the Buckingham potential. Unfortunately, the oxygen distortion that allows for 7-fold coordinated Zr cations is not stable with the potential and the oxygen revert back to their normal pyrochlore positions. That is, 7-fold coordinated Zr cations are not stable with the potential. Further, stabilizing such coordination states is challenging with these potentials, even though it is critical for describing the monoclinic structure of e.g. ZrO_2, possibly due to the fact that the charges on ions are static in these models. Despite this issue, we used the structure as an alternative ordering for $x = 0.75$ to better understand the impact of the Zr/Ti distribution on defect mobilities.

2.2 Dynamical Simulations

To examine the impact of chemical composition and ordering on defect mobility, we used temperature accelerated dynamics (TAD). TAD is one of a number of accelerated molecular dynamics (AMD) methods that, assuming rare events, allows for the simulation of much longer times than possible with standard molecular dynamics (MD), while still retaining the fidelity of the underlying interatomic interactions. TAD is the most approximate of the AMD methods, assuming that the rare events are described by harmonic transition state theory (HTST). Details of the TAD algorithm are described elsewhere[20,21]. A TAD simulation is governed by a (low) temperature of interest (T_{low}), a higher temperature to accelerate the occurrence of rare events (T_{high}), an assumed minimum prefactor in the system (ν_{min}), and a confidence factor that the correct events are chosen (δ). In the simulations reported here, we used TAD parameters of T_{low} =1500 K, T_{high} =2500 K, ν_{min} =10^{12}/s, and δ =0.05 (corresponding to a confidence level of 95%). The boost factors for these simulations were not large,

range from a factor of 4 over conventional MD to less than 1. However, it is critical to note that while the simulated time that was reached in those cases was smaller than could have been achieved with conventional MD, the TAD procedure also leads to the characterization of every possible event observed in the simulation, via the calculation of the energy barriers using the nudged elastic band (NEB) method[22]. Thus, this boost factor includes the cost of those NEB calculations and the effective boost of the entire simulation is still greater than what would have been achieved performing MD and characterizing the events in such an MD simulation.

The TAD simulations were based upon a Buckingham description of the interatomic interactions. Specifically, we used the parameterization developed by Minervini et al.[23]. As mentioned, this potential does not completely reproduce the behavior predicted by DFT calculations, particularly the stability of the 7-fold Zr polyhedra. However, it does describe the general trends of ordering and disordering found from DFT. Simulations using similar potentials for other systems (such as MgO[24] and perovskites[25]) reproduced behavior determined from either DFT calculations or experiment.

In this work, we added an extra oxygen vacancy to the system and followed the dynamics of that defect. In principle, the structural vacancies in pyrochlore should be mobile, but the time scale for that mobility, particularly at a temperature of T_{low} =1500 K, is still beyond the reach of TAD. Further, keeping the temperature low so that only the extra defect migrates allows us to better analyze the trajectory. If all of the structural vacancies were mobile, a detailed analysis of the migration pathways would be significantly more challenging. We note that all of these simulations were performed at the relaxed lattice constants of the respective structure as determined from the Monte Carlo. For the DFT-based simulation cell, the lattice constant was relaxed with the potential.

In generating trajectories for visualization, we tracked the center-of-mass of the vacancy. In cases where the vacancy is localized on specific lattice sites, this is trivial. However, for more complex structures, such as the split interstitials observed in the Zr rich compounds, we chose the location of the central interstitial as representative of the position of the vacancy complex. In rare cases, even more complex structures were formed, consisting of reconstructions that could include, for example, three vacancies and two interstitials. In these cases, we arbitrarily chose one of the interstitials to represent the center-of-mass of the complex. Finally, in defining defects, we used the reference lattice method[24] with a cutoff of one angstrom.

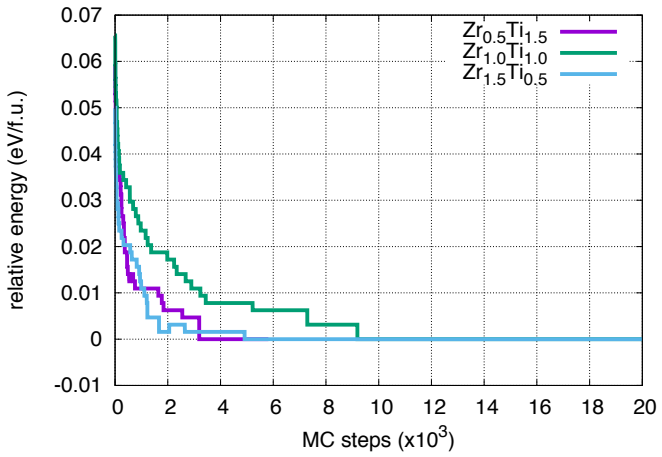

Fig. 1 Energy of the three pyrochlore compositions discussed in the text versus MC steps, going from a disordered distribution to an ordered distribution of Zr and Ti on the B sublattice of $Gd_2B_2O_7$.

3 Results

3.1 Structure of Ordered GTZO

As mentioned, three compositions were considered for the Monte Carlo (MC) simulations and a fourth structure for the $x = 0.75$ composition was taken from previous DFT calculations. The energy versus MC steps curves for the three systems generated using the empirical potential are shown in Fig. 1, highlighting the fact that they reach a state in which the energy is minimized versus the Zr/Ti distribution.

The final structures obtained from this procedure, along with that taken from our previous DFT calculations, are shown in Fig. 2. It is apparent that, in these structures, the B cations arrange in very specific manners. In the case of $x = 0.25$, the Ti and Zr ions arrange in alternating 110 planes, with dense planes of Ti separated by less dense planes of Zr ions. For the composition $x = 0.5$, the cations arrange in 100 planes, though this time the Zr planes are more dense and the Ti ions form columns in between Zr polyhedra along 110 directions. For the $x = 0.75$ composition, there are two structure. The first, structure A found via MC with the empirical potential, is a mirror to the $x = 0.25$ composition, with dense planes of Zr ions separated by sparse planes of Ti. In contrast, structure B, which was found from the DFT calculations, while still having an ordered structure, exhibits a more complex arrangement with a less obvious separation of the Ti and Zr ions. The Zr ions still form dense planes, but the Ti ions are arranged into more connected polyhedra than in structure A.

3.2 Oxygen Vacancy Migration

To understand the impact of the chemical composition and the resulting chemical ordering in $Gd_2(Ti_{1-x}Zr_x)_2O_7$ on defect trans-

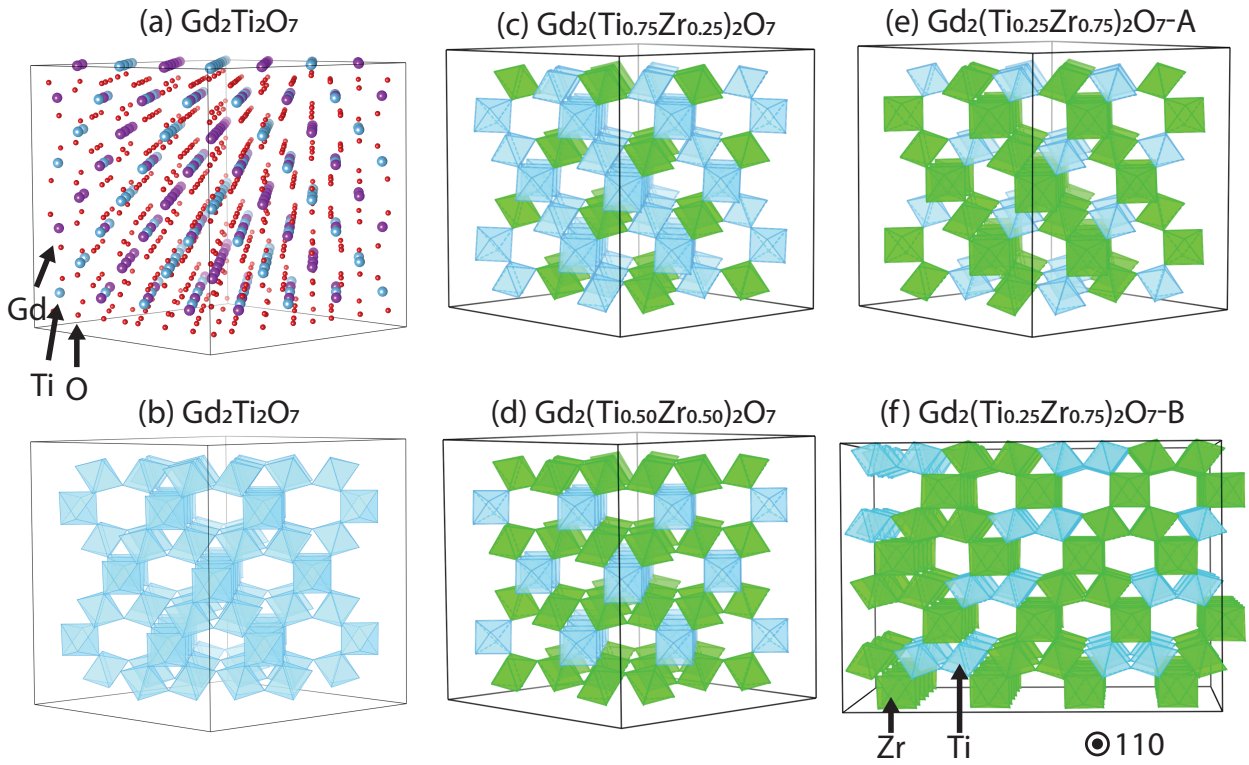

Fig. 2 The structure of (a-b) $Gd_2Ti_2O_7$ and (c-f) the final structures for mixed $Gd_2(Ti_{1-x}Zr_x)_2O_7$ pyrochlores. In (a), the red spheres are oxygen, the blue spheres are Ti, and the purple spheres are Gd. The structure of $Gd_2Ti_2O_7$ is shown both (a) atomically and (b) representing only the Ti polyhedra. In (b-f), the green polyhedra are coordination polyhedra for Zr ions while the blue polyhedra are those for Ti ions. Oxygen and Gd ions are not shown for clarity. Thus, the B cations are at the center of the respective polyhedra and the oxygen ions are at the vertices. Two structures are shown for the composition $Gd_2(Ti_{0.25}Zr_{0.75})_2O_7$ $(x = 0.75)$, one of which was found from MC simulations with the potential (structure A) and one that was found from DFT calculations (structure B).

port, we examined the kinetic evolution of an extra oxygen vacancy. As noted above, pyrochlores have an extensive network of structural oxygen vacancies, a consequence of the reduced valence of the A cations compared to the parent fluorite structure. These vacancies are responsible for the high conductivity that makes pyrochlores attractive as fast-ion conductors. However, particularly for compounds containing Ti which do not exhibit such high conductivity[26], these structural vacancies are not mobile on the timescale accessible via direct simulation for a temperature of T=1500 K. Thus, to induce defect mobility on the timescales we can reach, we introduce an extra or extrinsic oxygen vacancy into the system. We then track the kinetics of this vacancy during the course of TAD simulations.

We observe that the mobility of the oxygen vacancy is strongly influenced by the arrangement of the B cations. For example, in the case of $x = 0.25$, or the composition $Gd_2(Ti_{0.75}Zr_{0.25})_2O_7$ (the Ti rich composition examined here), the Ti ions are arranged along 110 planes of the structure. This is directly reflected in the trajectory of the oxygen vacancy, as shown in Fig. 3. Figure 3a highlights all of the positions that the oxygen vacancy visited during the course of the simulation. Clearly, there is a strong correlation between the position of the oxygen vacancy and the location of the Ti polyhedra. That the Ti polyhedra are arranged in 110 planes results in constrained migration of the oxygen vacancy. Specifically, the oxygen vacancy migration is confined to a plane, and thus exhibits two-dimensional diffusion. This is highlighted in Figs. 3b-c, which show the time-resolved trajectory along two different directions. The vacancy diffuses in a 110 plane, exhibited a random walk within that plane.

As the Zr content of the compound is increased, the migration of the oxygen is further constrained. In this case, the Ti ions are further isolated, forming one-dimensional chains along the 110 direction of the structure. Because of the strong affinity of the oxygen vacancy to the Ti ions, this again constrains the migration of the oxygen vacancy to a pseudo-one-dimensional nature, as shown in Fig. 4. As shown in Fig. 4a, the position of the oxygen vacancy is tightly constrained to just a few columns of Ti ions. This is more clearly illustrated in Fig. 4b, which shows the time-resolved trajectory of the vacancy. The vacancy migrates one-dimensionally along 110 chains of Ti, with relatively rare excursions that take it from one chain to a neighboring chain. Thus, migration of the oxygen vacancy in this structure would be much faster along the chains than perpendicular to them, resulting in predominantly one-dimensional migration.

As the Ti content is further reduced, the Ti ions become even more isolated. Depending on the specific arrangement of these Ti ions, the oxygen vacancy can become essentially immobilized in the structure. For example, in structure A for the composition $Gd_2(Ti_{0.25}Zr_{0.75})_2O_7$, the Ti polyhedra are completely surrounded by Zr polyhedra – they do not touch one another. As shown in Fig. 5, on the timescale of our simulation, we do not observe the oxygen vacancy leaving the vicinity of the initial Ti polyhedra. Essentially, compared to the more Ti rich compounds, the oxygen vacancy is immobilized in this structure.

Clearly, the mobility of the oxygen vacancy is tied to the connectivity of the Ti ions in the structure. For the same composition, if that connectivity is changed, the oxygen vacancy can again become mobile. In structure B for the composition $Gd_2(Ti_{0.25}Zr_{0.75})_2O_7$, there is greater connectivity between the Ti polyhedra. They do not form a connected chain through the structure, but pairs of polyhedra are connected. This is enough to induce migration of the oxygen vacancy on the nanosecond timescale, as shown in Fig. 6. The trajectories in this case are significantly more complex than in the previous simulations, with a less obvious connection to the Ti polyhedra. That is, the oxygen vacancy is now able to visit Zr polyhedra that are unconnected to Ti polyhedra. This leads to a seemingly two-dimensional migration pathway through the structure, as highlighted by Figs. 6b-c.

To quantify the relationship between the cation structure and the vacancy mobility, we examined the mean squared displacement (MSD) of the atoms as a function of time. These results are presented in Figure 7. Two trends can be gleaned from these plots. First, as the Zr content is increased, the MSD tends to decrease. This is reflected in the extracted diffusion constants D (from the fits to the MSD via the relationship $2Dt = MSD$), as summarized in Table 1. These diffusion constants must be taken qualitatively as, in particular for the case reflected in Fig. 7c, the trajectory over which the MSD is extracted is not very long. However, the extracted values of D do highlight the trends we qualitatively observed before. Further, they are in of a similar order of magnitude for what we found in the two end members from molecular dynamics (MD)[17] – 0.005 nm^2/ns for $Gd_2Zr_2O_7$ and 0.0004 nm^2/ns for $Gd_2Ti_2O_7$. (These values were found by extrapolating the results in Ref.[17] to 1500 K; it should be noted that those MD simulations were performed on simulation cells that were relaxed at the given temperature). It is interesting to note that the mobilities in our current work, except for the slowest case, are higher than either end member, suggesting that ordering not only modifies the dimensionality of the moving vacancy but also enhances the rate of migration. Figure 7 also highlights the barriers, measured relative to the global minimum energy found during the simulation, encountered during each trajectory. In the case of $x = 0.25$ (Fig. 7a), all of the barriers that describe net motion of the atoms are on the order of 0.8 eV. When $x = 0.5$ (Fig. 7b), the barriers for net atomic migration are larger, in the range of 1.2-1.5 eV. For $x = 0.75$, the two structures exhibit drastically different behavior. In the case of structure A (Fig. 7c), only two distinct "super-basins" are visited in the 90 ns of the trajectory shown. Further, to go from of the super-basins to the next

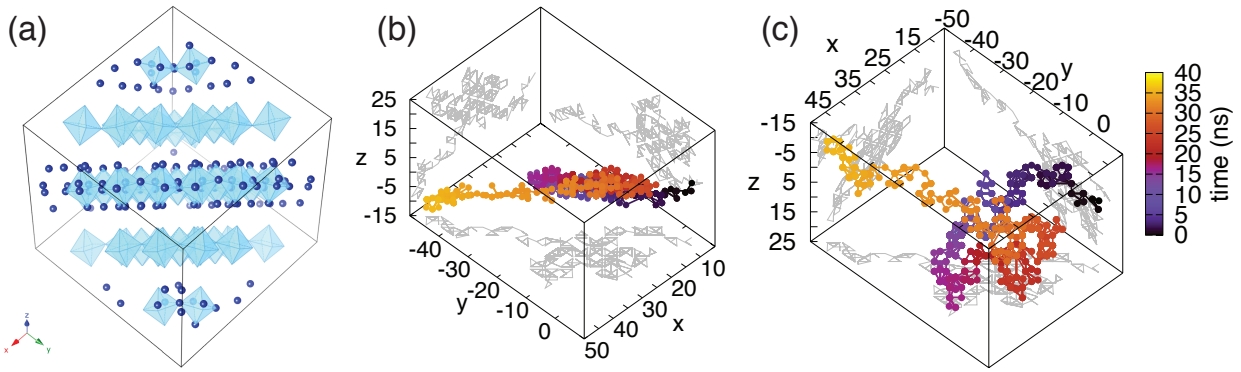

Fig. 3 The trajectory of an oxygen vacancy in $Gd_2(Ti_{0.75}Zr_{0.25})_2O_7$. (a) The time-collapsed position of the oxygen vacancy, highlighted by the dark blue spheres. In this image, only the Ti polyhedra are shown for clarity. (b-c) Two different perspectives of the time-resolved trajectory of the oxygen vacancy through the system. The color of the trajectory indicates the time at which the vacancy visited the indicated position in the simulation cell.

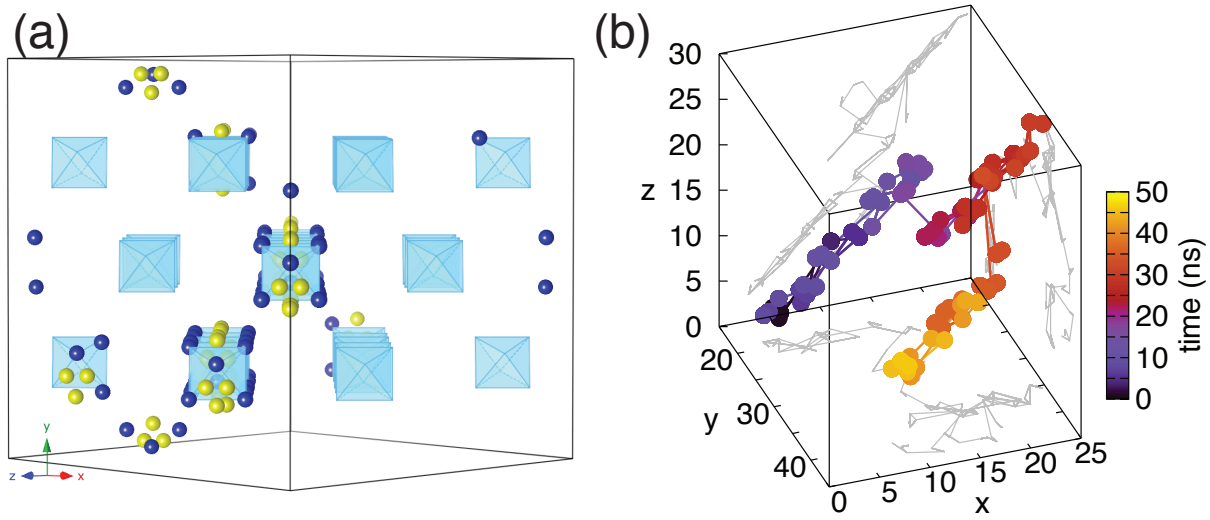

Fig. 4 The trajectory of an oxygen vacancy in $Gd_2(Ti_{0.5}Zr_{0.5})_2O_7$. (a) The time-collapsed position of the oxygen vacancy, highlighted by the dark blue spheres. For this composition, the oxygen vacancy often forms a split structure and the central oxygen "interstitial" is indicated by a yellow sphere. In this image, only the Ti polyhedra are shown for clarity. (b) The time-resolved trajectory of the oxygen vacancy through the system. The color of the trajectory indicates the time at which the vacancy visited the indicated position in the simulation cell.

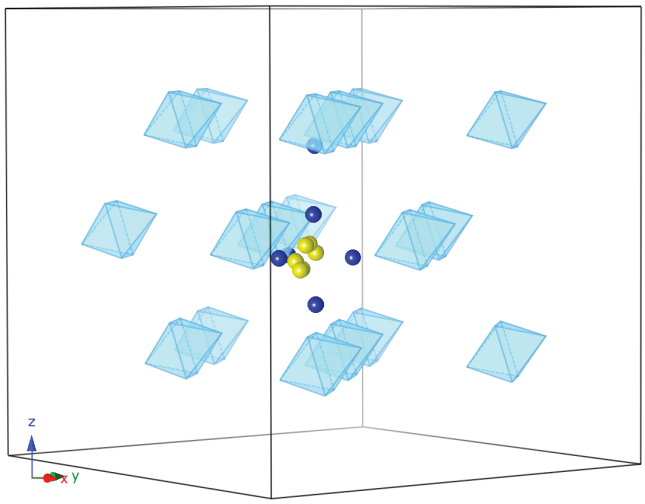

Fig. 5 The time-collapsed position of the oxygen vacancy, highlighted by the dark blue spheres, in structure A of $Gd_2(Ti_{0.25}Zr_{0.75})_2O_7$. For this composition, the oxygen vacancy often forms a split structure and the central oxygen "interstitial" is indicated by a yellow sphere. In this image, only the Ti polyhedra are shown for clarity.

Structure	Diffusion Constant (nm^2/ns)
$Gd_2(Ti_{0.75}Zr_{0.25})_2O_7$	0.27
$Gd_2(Ti_{0.5}Zr_{0.5})_2O_7$	0.073
$Gd_2(Ti_{0.25}Zr_{0.75})_2O_7$ A	0.0026
$Gd_2(Ti_{0.25}Zr_{0.75})_2O_7$ B	0.14

Table 1 Diffusion constants extracted by fitting the expression $2Dt = MSD$ to the MSD results in Figure 7.

requires a barrier of about 1.2 eV, while the barriers within the super-basins are relatively very small. In contrast, while super-basin behavior is also seen for structure B (Fig. 7d), the barriers within the super-basin are larger, about 0.8-1.0 eV. It still requires overcoming a barrier of closer to 1.2 eV (the larger yellow points in Fig. 7d) for net migration of the atoms. The distribution of the barriers in the various structures will be discussed in greater detail below.

4 Discussion

The TAD simulations discussed above reveal that the migration of defects, specifically of an extrinsic oxygen vacancy, is strongly influenced by the connectivity of Ti polyhedra in mixed $Gd_2(Ti_{1-x}Zr_x)_2O_7$ pyrochlores. The trajectories shift from three-dimensional in the single-component end members[27], to two-dimensional, pseudo-one-dimensional, to even essentially zero-dimensional depending on the composition. Further, for a given composition, the migration of the vacancy depends critically on the relative arrangement of the Ti and Zr ions (compare Figs. 5 and 6). Some of this interpretation is admittedly from relatively short-timescale simulations, and on long enough timescales at high enough temperatures, we would expect that the vacancy can diffuse completely through the crystal. However, we expect that the results presented here provide some insight into how the rate of that transport is affected by the chemical ordering.

This complexity is reflected in the energetics of the trajectory, as shown in Fig. 8. Figure 8a shows the energy of the states visited during the course of the TAD simulations for all four compositions. The lowest energy state for each case is shifted to zero energy. As might be expected from the complexity of the trajectories shown in Figs. 3-6, the cases with the more complex trajectories also have a more varied energy landscape. In particular, for the relatively simple trajectories for the $x = 0.25$ and $x = 0.5$ compositions, only two or three unique energy states are visited during the course of the runs. However, for structure B for the $x = 0.75$ composition, there is a much greater variety of states, a reflection of the greater number of environments the vacancy visits in the course of its trajectory. This complexity is also reflected in the barriers between these states, as highlighted in Figs. 8b-c. Figure 8b provides the barriers relative to the state being exitted, while Fig. 8c is the absolute energy of the barrier relative to the lowest energy state in the system, which is provided as this gives the same reference for barriers going forward and backward between two states, collapsing them to one value. While in the Ti rich compositions there are only a few barriers that dominate the dynamics of the trajectory, there is a much wider range of barriers for the Zr rich case (at least for structure B for which there is net migration of the vacancy).

The barrier information in Fig. 8c suggests that, in addition to the nature and the complexity of the trajectories changing with composition and cation distribution, so too does the rate of migration. The migration energies for the $x = 0.5$ composition are lower than for the $x = 0.25$ composition, indicating that the migration rate is faster for that composition. The situation for $x = 0.75$ is less clear, as there is a wide range of barriers and it is not so obvious which barriers are required for net migration and which describe rearrangements of the vacancy around a given lattice site. In structure A, the vacancy is unable to escape the environment of the original Ti polyhedron it is associated with, at least on the time scales of our simulations. This is partially due to a low-barrier effect, where there are a number of states that describe rearrangment of the vacancy in the vicinity of that polyhedron and there is some significantly larger barrier for it to break free. The fact that we do not see net migration of the oxygen vacancy in this case is at least partially due to this super basin effect[28]. This is reflected in the barrier distribution shown in Fig. 8c, which reveals that, of the four structures considered here, structure A has the lowest absolute barrier, a signature of the super basin. For

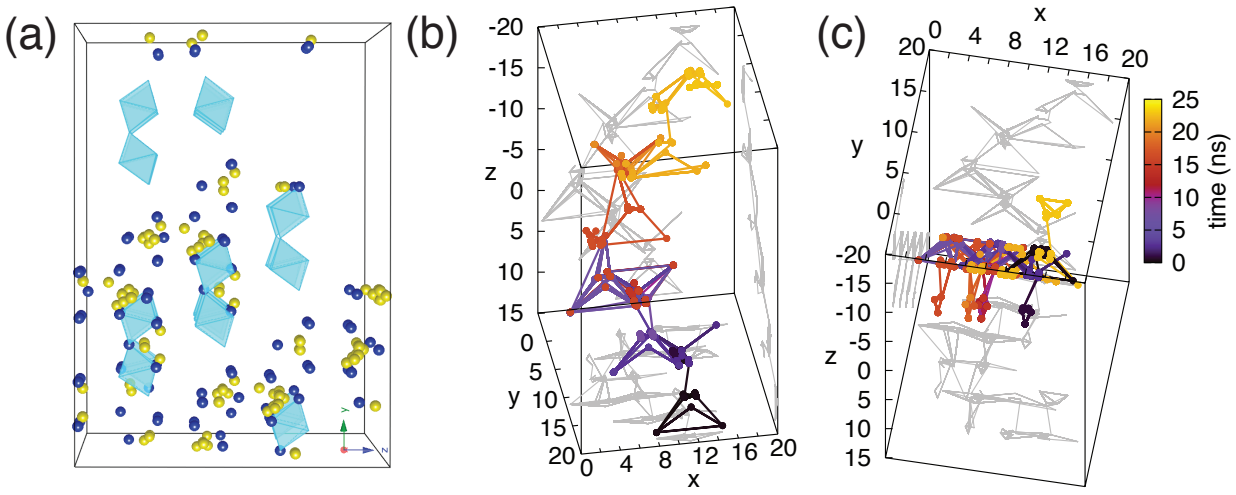

Fig. 6 The trajectory of an oxygen vacancy in structure B of $Gd_2(Ti_{0.25}Zr_{0.75})_2O_7$. (a) The time-collapsed position of the oxygen vacancy, highlighted by the dark blue spheres. For this composition, the oxygen vacancy often forms a split structure and the central oxygen "interstitial" is indicated by a yellow sphere. In this image, only the Ti polyhedra are shown for clarity. (b-c) Two different perspectives of the time-resolved trajectory of the oxygen vacancy through the system. The color of the trajectory indicates the time at which the vacancy visited the indicated position in the simulation cell.

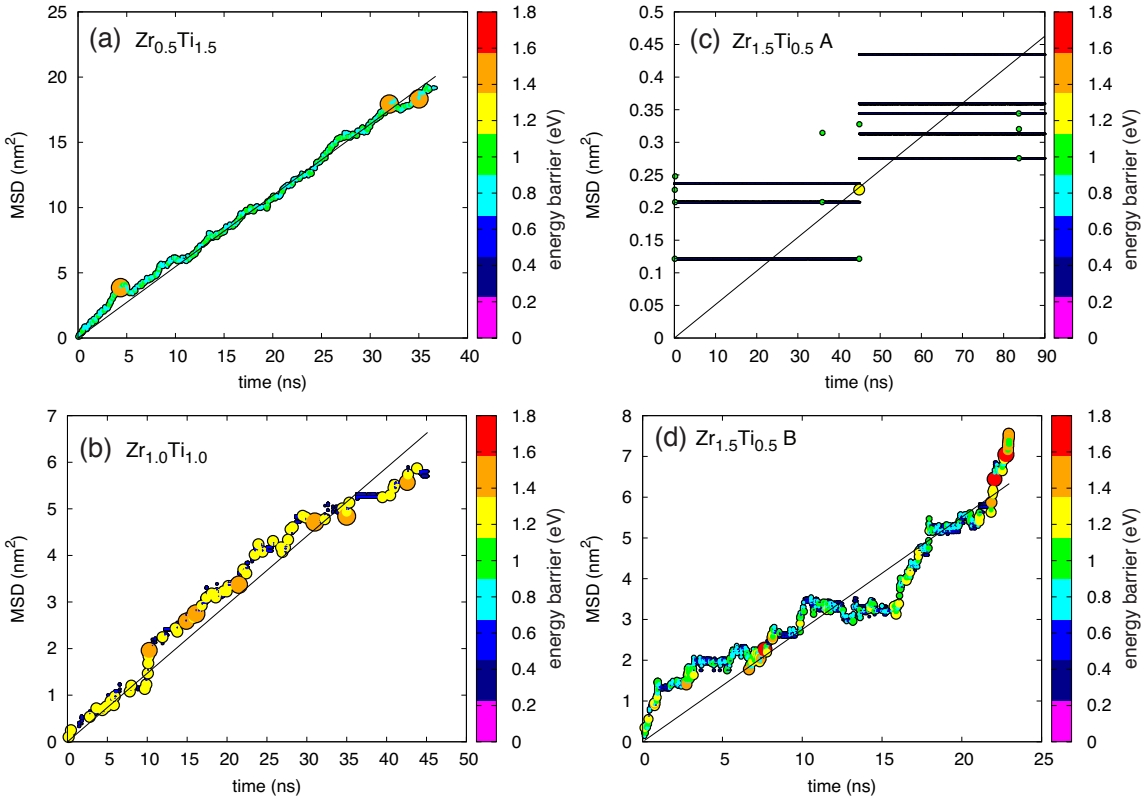

Fig. 7 The MSD of the atoms versus times in the four simulations described above. All MSDs are referenced to $t = 0ns$. The points represent the time at which an event occured and both the size and the color scale with the absolute energy of the barrier describing that event (with the relationship size/color energy[3], for clarity. The lines are linear fits to the MSD, the slope of which gives $2D$, with D being the diffusivity of the atoms during the course of the simulation. When the barriers are particularly small, they only appear as small dots in the figures. This is particularly evident in (c), where the overlapping barriers appear as horizontal lines.

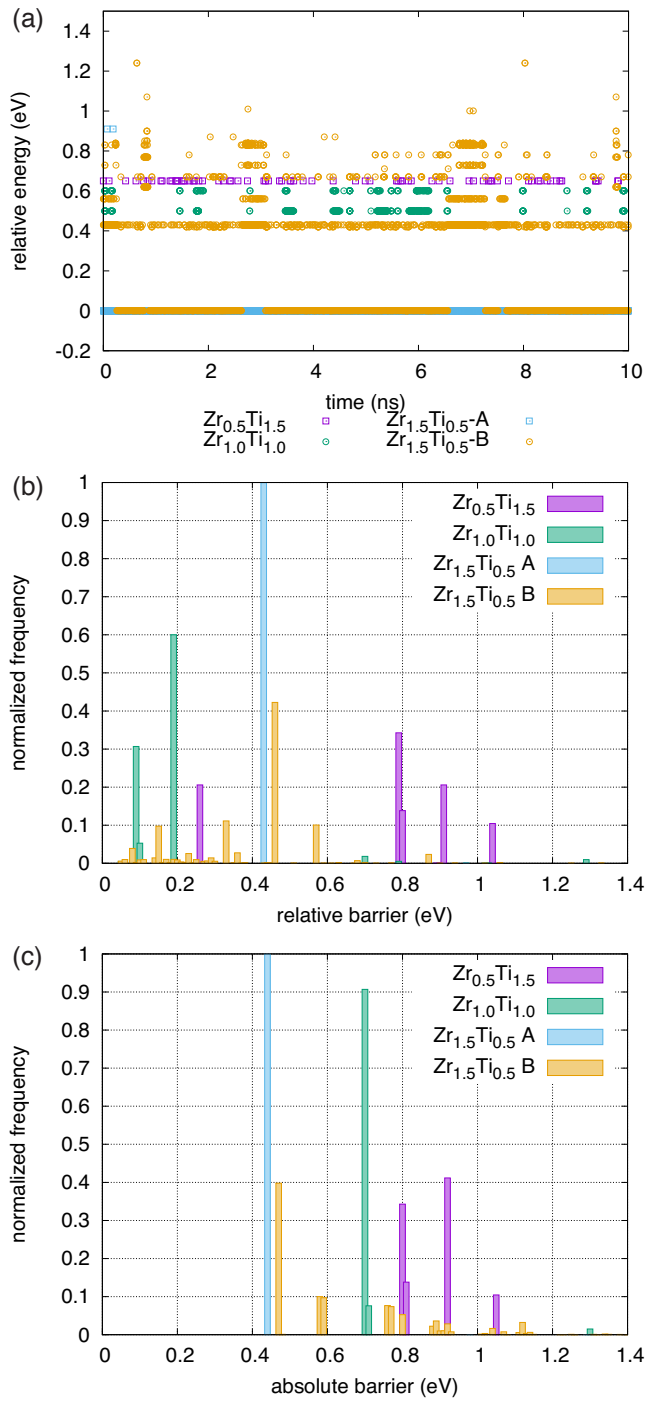

Fig. 8 Energetics associated with the trajectories from the TAD simulations. (a) The energy, relative to the lowest energy state in a given simulation, of the states visited during the course of each TAD simulation. Only the first 10 ns are shown, a time reached by each simulation. (b-c) The frequencies of the (b) relative and (c) absolute energies of the saddle energies as determined from NEB calculations during the TAD simulations. The frequencies are normalized to the total number of saddles visited during each simulation (so that the aggregate sums to 1).

structure B, the vacancy is able to overcome larger barriers and migrate through the system partially because there is a wider distribution of states with relatively smaller barriers between them.

It should be noted that, as the composition becomes Zr rich, the structure of the oxygen vacancy changes. In the Ti rich composition ($x = 0.25$), the oxygen vacancy is localized on a very specific oxygen lattice site. However, as the Zr content is increased, the oxygen vacancy structure becomes more complicated, typically taking on the structure of a split vacancy, with an oxygen ion being displaced into an interstitial site between two vacant lattice sites. These types of structures are illustrated in Fig. 9, which shows one migration pathway for the oxygen vacancy in structure B ($x = 0.75$). The lowest energy structure corresponds to one in which the vacancy is associated with a Ti polyhedron, consistent with the confinement of the vacancy to Ti in the other structures. However, as the vacancy migrates through the structure, it visits other environments, particulary one in which it is fully coordinated by Zr polyhedra.

Chemical mixing is often used to examine the impact of disorder on ionic conductivity[26,29,30]. Some pyrochlore chemistries prefer an ordered phase to a greater extent than others, so mixing two pyrochlore chemistries can induce different levels of ordering in the material. This allows for one approach to study the relationship between disorder and conductivity. Our results indicate that the migration of defects, where the oxygen vacancy is one representative example, is very sensitive to the detailed arrangement of those cations. The structures we have considered are very ordered, structures predicted to form in the mixed $Gd_2(Ti_{1-x}Zr_x)_2O_7$ pyrochlore at low temperature. Thus, they are not necessarily representative of the structures occuring in the experimental samples. That said, any heterogeneities in cation structure at the atomic scale will have important consequences for the migration of defects. Coupled with recent reports that these materials exhibit short-range order in the supposed disordered state[31,32] indicates that care should be taken when correlating transport properties with more macroscopic measurements of disorder or cation arrangements. Indeed, there is at least one report of ionic conductivity versus chemical composition that shows a non-monotonic dependency, suggesting that the chemical structure is not a simple random solid solution versus chemistry[16].

For the most part, we have only considered the behavior of the oxygen vacancy in one ordered structure at each composition. Here, we have essentially examined the ground state structure. In reality, for a given composition, there would be an ensemble of structures, depending on the temperature. At higher temperatures, other structures would become relevant and the behavior would be dictated by an ensemble average of those individual behaviors. Indeed, the effects of entropy, both vibrational and configurational, on the behavior of chemically complex systems has shown these effects to be important[33,34]. Thus, there is clearly

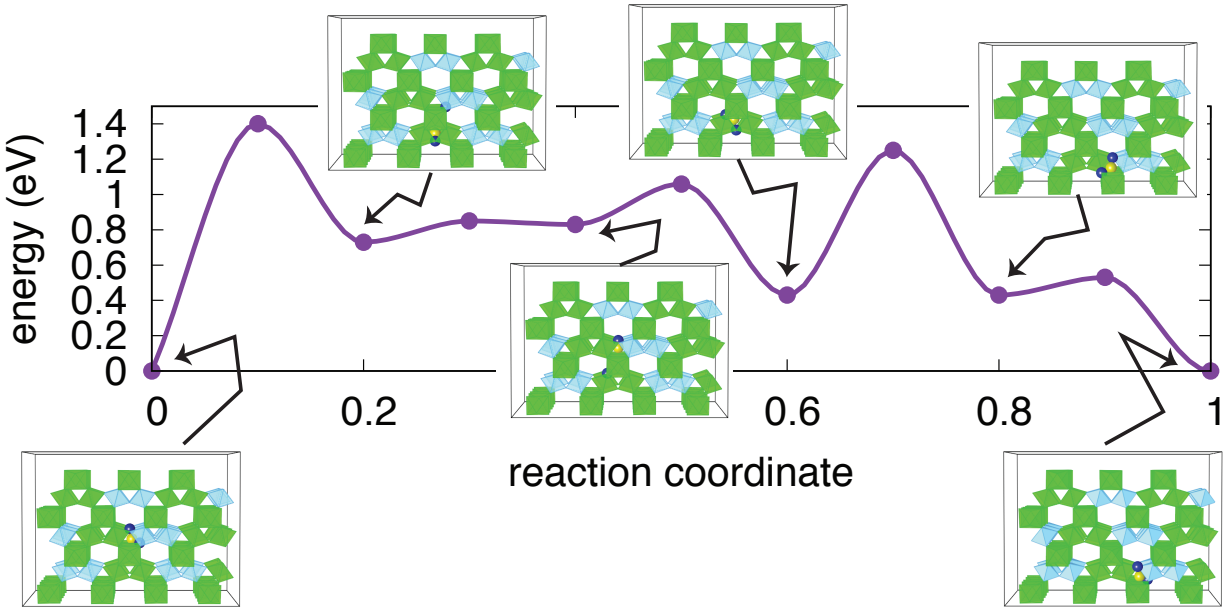

Fig. 9 One migration pathway for an oxygen vacancy in structure B for the composition $x = 0.75$. The color scheme is similar to previous figures.

a need to consider this problem more completely to understand the effects of temperature on the structure and, consequently, the transport. Similarly, there are questions about the inherent stability of a given mixed pyrochlore as a function of composition and chemistry. Just as has been done for other materials[35,36], models that examine the relative stability of different structures versus mixing or phase decomposition can be built. In fact, in our previous work[10], we attempted precisely that exercise for this materials system. However, the strong off-lattice nature of the relaxations precluded the construction of a reasonable cluster expansion model. Thus, while it would be valuable to identify the dominant structure(s) as a function of temperature and composition and thus the transport properties as a function of those variables, this is a significant undertaking that is beyond the scope of the present work.

That said, our results reveal that there is potential untapped opportunity for tuning the properties of complex oxides such as pyrochlores in the same way that has been explored for simpler structures such as perovskites. For example, the transport properties are clearly very sensitive to the detailed arrangement of cations and, to the extent that specific orderings can be realized in experiment, control of cation structure offers one way of controlling the transport properties in these materials. However, beyond this, just as other properties such as the band gap are sensitive to the composition and ordering in double perovskites[37], they should be tunable by changing the composition of pyrochlores. Given the wide range of potential application of pyrochlores, ranging from fast-ion conductors[38] to nuclear waste forms[39] to spin-ice materials[40] to catalysts[41], the potential impact of mixed pyrochlores is significant.

5 Conclusions

To conclude, we have used temperature accelerated dynamics to examine the mobility of oxygen vacancies in ordered $Gd_2(Ti_{1-x}Zr_x)_2O_7$ mixed pyrochlores for multiple compositions (values of x) and, for one composition, two different distributions of cations. We find that the nature of the trajectory of the defect is very sensitive to the distribution of cations. In particular, the connectivity of Ti polyhedra is critical in determining both the dimensionality of the trajectory as well as the rate of migration. Our results indicate that the detailed cation distribution strongly dictates the transport characteristics of the material. While we have only considered ordering on the B sublattice, we expect that the trends are more general and would also apply to pyrochlores in which mixing occurs on both the A and B sublattices. Our results suggest that care must be taken when trying to correlate transport properties, such as conductivity, with global measures of cation distributions, such as those obtained from x-ray diffraction. Rather, the nature of the short-range order should also be considered when interpretting such experiments.

Acknowledgements

The authors thank the group of Richard G. Hennig for help in orthogonalizing the DFT structure used in this work. This work was supported by the U.S. Department of Energy, Office of Science, Basic Energy Sciences, Materials Sciences and Engineering

Division. This work was supported by the US Department of Energy through the Los Alamos National Laboratory. Los Alamos National Laboratory is operated by Triad National Security, LLC, for the National Nuclear Security Administration of U.S. Department of Energy (Contract No. 89233218CNA000001).

References

1 T. Ishihara, H. Matsuda and Y. Takita, *Journal of the American chemical society*, 1994, **116**, 3801–3803.

2 H. Hayashi, H. Inaba, M. Matsuyama, N. Lan, M. Dokiya and H. Tagawa, *Solid State Ionics*, 1999, **122**, 1–15.

3 C. E. Mohn, N. L. Allan, C. L. Freeman, P. Ravindran and S. Stølen, *Journal of Solid State Chemistry*, 2005, **178**, 346–355.

4 M. Van Dijk, K. De Vries and A. Burggraaf, *Solid State Ionics*, 1983, **9**, 913–919.

5 B. J. Wuensch, K. W. Eberman, C. Heremans, E. M. Ku, P. Onnerud, E. M. Yeo, S. M. Haile, J. K. Stalick and J. D. Jorgensen, *Solid State Ionics*, 2000, **129**, 111–133.

6 R. A. De Souza, *Journal of Materials Chemistry A*, 2017, **5**, 20334–20350.

7 G. King, S. Thimmaiah, A. Dwivedi and P. M. Woodward, *Chemistry of Materials*, 2007, **19**, 6451–6458.

8 S. Vasala and M. Karppinen, *Progress in Solid State Chemistry*, 2015, **43**, 1–36.

9 B. P. Uberuaga and G. Pilania, *Chemistry of Materials*, 2015, **27**, 5020–5026.

10 G. Pilania, B. Puchala and B. P. Uberuaga, *npj Computational Materials*, 2019, **5**, 7.

11 B. Mandal, A. Banerji, V. Sathe, S. Deb and A. Tyagi, *Journal of Solid State Chemistry*, 2007, **180**, 2643–2648.

12 M. Hirayama, N. Sonoyama, A. Yamada and R. Kanno, *Journal of Luminescence*, 2008, **128**, 1819–1825.

13 S. W. Reader, M. R. Mitchell, K. E. Johnston, C. J. Pickard, K. R. Whittle and S. E. Ashbrook, *The Journal of Physical Chemistry C*, 2009, **113**, 18874–18883.

14 K. R. Whittle, L. M. Cranswick, S. A. Redfern, I. P. Swainson and G. R. Lumpkin, *Journal of Solid State Chemistry*, 2009, **182**, 442–450.

15 A. Fernandes, D. McKay, S. Sneddon, D. M. Dawson, S. Lawson, R. Veazey, K. R. Whittle and S. E. Ashbrook, *The Journal of Physical Chemistry C*, 2016, **120**, 20288–20296.

16 C. Heremans, B. J. Wuensch, J. K. Stalick and E. Prince, *Journal of Solid State Chemistry*, 1995, **117**, 108–121.

17 R. Perriot and B. P. Uberuaga, *Journal of Materials Chemistry A*, 2015, **3**, 11554–11565.

18 R. Perriot, B. P. Uberuaga, R. J. Zamora, D. Perez and A. F. Voter, *Nature communications*, 2017, **8**, 618.

19 K. Mathew, A. K. Singh, J. J. Gabriel, K. Choudhary, S. B. Sinnott, A. V. Davydov, F. Tavazza and R. G. Hennig, *Computational Materials Science*, 2016, **122**, 183–190.

20 M. R. Sorensen and A. F. Voter, *J. Chem. Phys.*, 2000, **112**, 9599.

21 R. J. Zamora, B. P. Uberuaga, D. Perez and A. F. Voter, *Annual review of chemical and biomolecular engineering*, 2016, **7**, 87–110.

22 G. Henkelman, B. P. Uberuaga and H. Jónsson, *J. Chem. Phys.*, 2000, **113**, 9901.

23 L. Minervini, R. W. Grimes and K. E. Sickafus, *Journal of the American Ceramic Society*, 2000, **83**, 1873–1878.

24 B. P. Uberuaga, R. Smith, A. R. Cleave, F. Montalenti, G. Henkelman, R. W. Grimes, A. F. Voter and K. E. Sickafus, *Physical Review Letters*, 2004, **92**, 115505.

25 B. P. Uberuaga and L. J. Vernon, *Solid State Ionics*, 2013, **253**, 18–26.

26 H. L. Tuller, *Journal of Physics and Chemistry of Solids*, 1994, **55**, 1393–1404.

27 B. P. Uberuaga and K. E. Sickafus, *Computational Materials Science*, 2015, **103**, 216–223.

28 D. Perez, T. Vogel and B. P. Uberuaga, *Physical Review B*, 2014, **90**, 014102.

29 J. A. Díaz-Guillén, A. F. Fuentes, M. R. Díaz-Guillén, J. M. Almanza, J. Santamaría and C. León, *Journal of Power Sources*, 2009, **186**, 349 – 352.

30 K. J. Moreno, A. F. Fuentes, M. Maczka, J. Hanuza, U. Amador, J. Santamaría and C. León, *Physical Review B*, 2007, **75**, 184303.

31 J. Shamblin, M. Feygenson, J. Neuefeind, C. L. Tracy, F. Zhang, S. Finkeldei, D. Bosbach, H. Zhou, R. C. Ewing and M. Lang, *Nature materials*, 2016, **15**, 507.

32 D. Simeone, G. J. Thorogood, D. Huo, L. Luneville, G. Baldinozzi, V. Petricek, F. Porcher, J. Ribis, L. Mazerolles, L. Largeau *et al.*, *Scientific reports*, 2017, **7**, 3727.

33 T. Zhu and E. Ertekin, *Energy & Environmental Science*, 2019, **12**, 216–229.

34 W.-M. Choi, Y. H. Jo, S. S. Sohn, S. Lee and B.-J. Lee, *npj Computational Materials*, 2018, **4**, 1.

35 D. Fuks, S. Dorfman, S. Piskunov and E. Kotomin, *Physical Review B*, 2005, **71**, 014111.

36 D. Fuks, Y. Mastrikov, E. Kotomin and J. Maier, *Journal of Materials Chemistry A*, 2013, **1**, 14320–14328.

37 G. Pilania, A. Mannodi-Kanakkithodi, B. Uberuaga, R. Ramprasad, J. Gubernatis and T. Lookman, *Scientific reports*, 2016, **6**, 19375.

38 T. Norby, *Journal of Materials Chemistry*, 2001, **11**, 11–18.

39 W. Weber, R. Ewing, C. Catlow, T. D. De La Rubia, L. Hobbs, C. Kinoshita, H. Matzke, A. Motta, M. Nastasi, E. Salje *et al.*,

Journal of Materials Research, 1998, **13**, 1434–1484.

40 S. T. Bramwell and M. J. Gingras, *Science*, 2001, **294**, 1495–1501.

41 J. Goodenough and R. Castellano, *Journal of Solid State Chemistry*, 1982, **44**, 108–112.